Journal of Materials Chemistry B

Accepted Manuscript

ROYAL SOCIETY OF CHEMISTRY

www.rsc.org/materialsB

Cite this: DOI: 10.1039/c0xx00000x

www.rsc.org/xxxxxx

ARTICLE TYPE

Hybrid lanthanide nanoparticles as a new class of binary contrast agents for *in vivo* T_1/T_2 dual-weighted MRI and synergistic tumor diagnosis

Zhigao Yi,[a,b,d] Xiaolong Li,[a,d] Wei Lu,[c] Hongrong Liu,[a] Songjun Zeng,[*a] and Jianhua Hao[*c]

Received (in XXX, XXX) Xth XXXXXXXXX 20XX, Accepted Xth XXXXXXXXX 20XX

DOI: 10.1039/b000000x

Lanthanides nanoparticles (NPs) known as upconversion fluorescent probes for multi-modal bioimaging including magnetic resonance imaging (MRI) have attracted much attention. In MRI, conventional contrast agents generally present separately in a single type of MRI. Single T_1- or T_2-weighted MRI has its unique limitations, thereafter it is urgent to combine the two modalities capable of providing more comprehensive and synergistic diagnostic information over the single modality of MRI. Unfortunately, there is a lack of such advanced materials as enhancing agents fully suitable for dual-modal MRI. Herein, we report a new class of hybrid lanthanide nanoparticles as synergistic contrast agents in T_1/T_2 dual-weighted MRI and the imaging directed tumor diagnosis. The r_2/r_1 value of pure $BaGdF_5$ NPs can be readily adjusted from 2.8 to 334.8 by doping 0, 50, or 100 % of Ln^{3+} (Ln^{3+} = Yb^{3+}, Er^{3+}, or Dy^{3+}), respectively. Among them, $BaGdF_5$:50 %Er^{3+} NPs are successfully used as binary-contrast agents for T_1/T_2 dual-weighted MRI and synergistic tumor diagnosis *in vivo*. These findings reveal that the longitude and transverse relaxivities of these Gd^{3+}-based NPs can be controlled by tuning Ln^{3+} dopants and their concentrations, providing a simple and general method and platform for designing simultaneous T_1/T_2 enhancing agents.

1. Introduction

MRI, as one of the most powerful and noninvasive diagnosis techniques in clinical and biomedical applications, has triggered intensive research interests in early test of many diseases, which is ascribed to its high spatial resolution, noninvasive diagnostic manner, and no restriction of penetration based on interaction of water protons with surrounding molecules of tissues.[1-7] Contrast signal of MRI images can be enhanced by the introduction of appropriate contrast agents. MRI contrast agents are utilized to change relaxation rate of water protons and thereafter to realize enhanced visualization effect between the focus of infection and normal tissues. In MRI, there are two principal processes, namely longitudinal and transverse relaxation corresponding to T_1 recovery (spin-lattice) and T_2 decay (spin-spin), respectively. T_1 recovery causes positive (or bright) MRI signal, while T_2 decay generates negative (or dark) images. The commonly used T_1 agents usually comprise paramagnetic complexes containing gadolinium (Gd^{3+}), iron (Fe^{3+}) or manganese (Mn^{2+}) ions.[8-16] However, these relatively small molecules generally have a short circulating time in vascular system within a few minutes because of their fast renal excretion, which is stumbling block to capture high-resolution MRI images. Superparamagnetic iron oxide nanoparticles (SPIONs) have been used as T_2 weighted contrast enhancing agents owing to their freedom from strong magnetic interactions in dispersion and high stability under physiology conditions.[17-22] Nonetheless, diagnosis confusion appears between lesions labeled by T_2 contrast agents and other low-level background areas, especially when the signal-to-noise ratio is low.[23-26]

T_1- or T_2-weighted contrast agents possess not only their own unique merits but great limitations. Therefore, integrating two modalities of MRI may provide more comprehensive and synergistic diagnostic information over the single modality.[21,27-36] Furthermore, compared with other multi-modal imaging, the development of T_1/T_2 dual-weighted MRI strategies in a single instrumental system could efficiently eliminate from image matching difficulties resulting from reloading of samples, depth penetration, and spatial/time resolution of multiple imaging systems, and further improve diagnostic accuracy to disease. Therefore, the development of new-type and suitable dual-weighted contrast agents suffers an urgent demand. Some nanomaterials exhibit intrinsic T_1/T_2 contrast effects in dual-weighted MRI. Ultra-small SPIONs (about 3 nm in diameter) exhibit great potential as T_1 contrast agents, while the T_2 contrast effects are weak.[11] In addition, the reported FeCo nanoparticles (NPs) system shows high T_1/T_2 contrast effects, but there is a lack of understanding the mechanism behind the observed effects.[20] Both Gd^{3+}-labeled magnetite (Fe_3O_4) NPs and SPIONs were used as dual-contrast agents for T_1/T_2 dual-weighted MRI.[32-36]

In spite of Gd^{3+} as T_1 agents, it is noticeable that other lanthanide ions (Ln^{3+}), e.g., Dy^{3+}, Ho^{3+}, Er^{3+}, Tm^{3+}, and Yb^{3+}, present relatively short transverse relaxation time, resulting in T_2 contrast effects.[37-40] While these Ln^{3+} ions are generally known for their upconversion luminescent properties, which provides strategies for designing multi-functional bioprobes in bioimaging,

e.g., upconversion optical imaging, computed tomography (CT), MRI, etc.[41-48] So far, most of Ln^{3+}-based nanomaterials have been studied as contrast agent for single-weighted MRI while only a few works have been focused on T_1/T_2 dual-contrast agents.[49] Recently, silica-coated core-shell upconversion nanostructures were employed as T_1/T_2 dual-weighted contrast agents, wherein both the longitudinal (r_1, $1/T_1$) and transverse (r_2, $1/T_1$) relaxivities have been optimized just via tuning the thickness of the silica shell.[49a] However, the multiple synthesis and surface modification procedures increase the difficulties of precise control of particle size. Therefore, it is significantly important to develop a simple and facile strategy for synthesizing new and ideal T_1/T_2 dual-weighted contrast agents using Ln^{3+} ions. Hydrothermal reaction used herein is considered as facile and universal method in fabricating Ln^{3+}-doped NPs with well dispersity and narrow size distribution.[50-52] The relaxation proton majorly affects T_2-weighted MRI through a so-called Curie mechanism, which contributes to increase substantially with the external magnetic field and is proportional to the square of the effective magnetic moment of Ln^{3+}.[53] Doping other Ln^{3+} into Gd^{3+}-hosted NPs can efficiently change transverse relaxivities, and as a result, can achieve optimization of both longitudinal and transverse relaxivities of NPs, as shown in Figure 1a.

In this work, $BaGdF_5$: x%Ln^{3+} (x = 0, 50, or 100; Ln^{3+} = Dy^{3+}, Er^{3+}, or Yb^{3+}) NPs were synthesized to study the variation of relativities of Gd^{3+}-based NPs via Ln^{3+} doping. These Ln^{3+} ions are selected because of their wide range of magnetic moments (Dy^{3+}, μ_{eff} = 10.63 μ_B, high; Er^{3+}, μ_{eff} = 9.59 μ_B, mediate; Yb^{3+}, μ_{eff} = 4.53 μ_B, low).[54,55] Oleate capping ligands of NPs are removed via a hydrochloric acid treatment to eliminate the quenching contribution from an inner-sphere mechanism.[41-48,56] As expected, optimization of relaxivities is easily realized through Ln^{3+} doping. Note that the as-obtained $BaGdF_5$: 50%Er^{3+} NPs show synergistic contrast effects in dual-weighted MRI and their tumor detection. This is the first time for demonstrating T_1/T_2 dual-weighted MRI and synergistic diagnosis of tumor using these designed binary contrast agents in single phase host, which provides a general Ln^{3+}-doping method for constructing dual-modal T_1/T_2 probes in single host with tunable r_2/r_1 values. It should be mentioned that $BaGdF_5$:Yb, Er has proved to be an excellent upconversion fluorescent label in our previous study.[47] Therefore, as multifunctional materials, these hybrid lanthanides NPs should be very useful in the area of multi-modal bioimaging.

2. Experimental

2.1 Chemicals and Materials

All reagents were of analytical purity and used without further purification. $LnCl_3 \cdot 6H_2O$ (99.99%, Ln^{3+} = Dy^{3+}, Er^{3+}, Yb^{3+}, and Gd^{3+}), and oleic acid (OA) were purchased from Sigma-Aldrich. $BaCl_2$, NaOH, and NH_4F and other regents were bought from Sinopharm Chemical Reagent Co., China.

2.2 Synthesis of OA-capped NPs

$BaGdF_5$: x mol%Ln^{3+} (x = 0, 50, or 100; Ln^{3+} = Dy^{3+}, Er^{3+}, or Yb^{3+}) NPs were prepared by a hydrothermal method utilizing OA as stabilizing agents. In a typical process,[52] 1.5 mL of NaOH solution (0.4 g/mL) was mixed with 10 mL of ethanol followed by addition with 20 mL of OA. After forming a transparent homogeneous mixture, 1 mL of $BaCl_2$ solution (1.0 M), 0.5 mmol of $GdCl_3$, and 0.5 mmol of $LnCl_3$ (Ln^{3+} = Dy^{3+}, Er^{3+}, or Yb^{3+}) were added in the above solution. After that, 6 mL of NH_4F aqueous solution (1.0 M) was added slowly. All these processes aforementioned were under vigorous stirring. After 30 min agitation, the obtained mixture was transferred into a 50 mL stainless Teflon-lined autoclave. The reaction system was sealed and maintained at 200 °C for 24 h. After reaction, the system was cooled to room temperature naturally. The samples were separated by centrifugation and washed with ethanol and de-ionized (DI) water in sequence for 3 times. Products were dried in air at 60 °C for a whole day.

2.3 Synthesis of ligand-free NPs

OA-capped NPs were converted to hydrophilic one using a HCl treated method. In a typical method,[57] 100 mg of OA-capped NPs was added into 20 mL of DI water. The solution was then under agitation for 2 h after tuning the pH value at 4 using dilute HCl solution. As a consequence, the carboxylate groups of the oleate ligand were removed. And then, two layers (ether and water layers) were formed by adding diethyl ether into the clarified solution and oleic acid in water layer was completely extracted for several times. Ligand-free NPs were then precipitated in acetone and collected by centrifugation and finally dispersed in DI water and used as contrast agents for further biomedical investigation.

2.4 Characterizations

XRD patterns were measured by a D/max-γA system X-ray diffractometer at 40 kV and 250 mA with Cu-Kα radiation (λ = 1.54056 Å). Microstructure studies were demonstrated by TEM, SAED, and HR-TEM via a JEM-2100F TEM equipped with an Oxford Instrument EDS system using an accelerating voltage of 200 kV.

2.5. Cytotoxicity assay

The cell cytotoxicity *in vitro* of $BaGdF_5$:50 mol%Er^{3+} NPs NPs in HeLa cells was measured via a MTT proliferation assay method. HeLa cells were cultured in Dulbecco's Modified Eagle Medium (DMEM) containing 10% fetal bovine serum, 1% penicillin and streptomycin at 37 °C and with 5% CO_2. Hela cells were transferred into a 96-well cell culture plate at 10^6 per well and incubated at 37 °C and with 5% CO_2 atmosphere for 24 h. Ligand-free $BaGdF_5$:50 mol%Er^{3+} NPs with different concentration (0, 50, 100, 250, and 500 μg/mL) were added into the wells in the absence of serum. Microscope observation was executed after another 4 h incubation of the wells at 37 °C and with 5% CO_2. Cell viability was calculated by a typical MTT assay. The procedures of MTT assay using HEK-293 cells are similar with the ones using Hela cells.

2.6. *In vitro* hemolysis assay

The hemolysis assay was conducted as an important factor to evaluate the *in vitro* biocompatibility.[58,59] Human blood samples stabilized with ethylene diamine tetraacetic acid (EDTA) were obtained from the local hospital. Firstly, 1 mL of blood sample was added into 2 mL of PBS, and then red blood cells (RBCs) were isolated from serum by centrifugation. The purified blood after washing was diluted to 1/10 of its original volume with

PBS. Diluted RBC suspension was mixed with PBS as negative control, with DI water as positive control, and with $BaGdF_5$:50 mol%Er NPs suspensions at differernt concentrations (0-200 μg/mL). And then the mixtures were centrifuged after 3 h. The absorbance of supernatants at 541 nm was detected by using a UV-vis spectroscope. The hemolysis percentage of RBCs was calculated as follows: percent hemolysis = [(sample absorbance - negative control absorbance)/(positive control absorbance - negative control absorbance)] ×100.

2.7 T_1/T_2 dual-weighted MRI *in vitro*

In vitro dual-weighted MRI images were acquired using a 1.5 T MRI system (HT-ANNMR-50, Shanghai Shinning Global Scientific and Educational Equipment Co.). Aqueous solutions containing ligand-free NPs with well-designed Gd^{3+} or Ln^{3+} (Ln^{3+} = Dy^{3+}, Er^{3+}, or Yb^{3+}) concentrations were transferred into 1.0 mL tubes for *in vitro* T_1 and T_2 MRI. The phatom images were performed using spin echo sequence in both *in vitro* T_1 and T_2 MRI. T_1-weighted sequence: Time of Repetition (TR) = 100 ms, Time of Echo (TE) = 10.6 ms, Matrix = 512 × 256, Field of View (FOV) = 50 × 130, Slice Thickness (ST) = 0.5 mm. T_2-weighted sequence was performed as follows: TR = 10 s, TE = 65 ms, matrix = 512 × 256, FOV = 50 × 130, ST = 0.5 mm. T_1 and T_2 relaxation times were conducted by inversion recovery sequence and spin echo sequence, respectively. Relaxivity values (r_1 or r_2) were calculated using the linear fitting of $1/T_1$ or $1/T_2$ relaxation times as a function of Gd^{3+} or Ln^{3+} (Ln^{3+} = Dy^{3+}, Er^{3+}, or Yb^{3+}) concentration, respectively.

2.8 Synergistic T_1/T_2 dual-weighted MRI *in vivo*

All animal procedures were in agreement with the institutional animal use and care regulations approved by the Laboratory Animal Center of Hunan Province. *In vivo* T_1 and T_2 dual-weighted MRI were conducted on a 1.0 T MRI scanner (Aspect Imaging, M3 MRI system) and their images were captured before and after administration of these hydrophilic NPs at different time points. Briefly, Kunming mice were firstly anesthetized via intraperitoneal injection with 150 μL of pentobarbital sodium aqueous solution (10 wt%) and then intravenously injected with 50 μL of aqueous solution containing ligand-free $BaGdF_5$:50 mol%Er^{3+} NPs (1.2 mM Gd^{3+} concentration). *In vivo* T_1- and T_2-weighted MRI was performed using the similar sequences like aforementioned *in vitro* test. Coronal cross-sectional images were captured before and at 30 min and 3 h after injection of NPs.

2.9 Synergistic detection of tumor in dual-weighted MRI

To further validate the dual-weighted high-contrast capabilities of these hydrophilic $BaGdF_5$:50 mol%Er^{3+} NPs, the tumor-bearing mice models were established for synergistic detection of tumor using T_1 and T_2 dual-weighted MRI. HeLa cells (1×10^7) were suspended in 50 μL of phosphate buffer saline solution and implanted into BALB/C mice by subcutaneous injection. *In vivo* tumor imaging was performed using the implanted mice after two weeks rearing under germ-free conditions. The inoculated tumor modals were intraperitoneally injected 150 μL of pentobarbital sodium aqueous solution (10 wt%) and then intravenously injected 50 μL of aqueous solution containing ligand-free $BaGdF_5$:50 mol%Er^{3+} NPs (1.2 mM Gd^{3+} concentration) from tail vein. Synergistic detection of tumor utilizing T_1 and T_2 dual-weighted MRI modalities were captured before and at 3 h after intravenous injection of NPs.

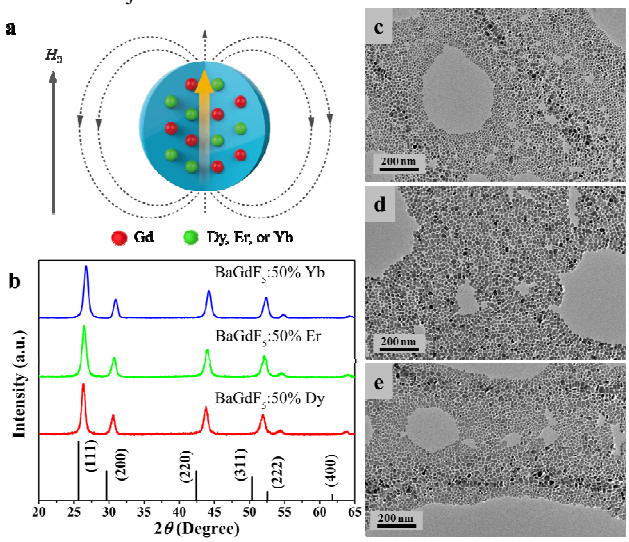

Figure 1. Structural representation and characterization of NPs. (a) Longitudinal and transverse relaxivities optimization of T_1/T_2 dual-weighted MRI contrast agents via doping other Ln^{3+} (Ln^{3+} = Dy^{3+}, Er^{3+}, or Yb^{3+}) into $BaGdF_5$ host. (b) XRD patterns of $BaGdF_5$:50 mol%Ln^{3+} (Ln^{3+} = Dy^{3+}, Er^{3+}, or Yb^{3+}) NPs and standard card of cubic phase $BaGdF_5$ crystal (JCPDS file No. 24-0098). (c-e) Representative TEM images of $BaGdF_5$:50 mol%Ln^{3+} (Ln^{3+} = Dy^{3+}, Er^{3+}, or Yb^{3+}) NPs, respectively.

3. Results and Discussion

3.1 Phase and Microstructure Characterization

To investigate optimization of longitude and transverse relaxivities of $BaGdF_5$ NPs via doping different Ln^{3+}, $BaGdF_5$ NPs doped with 0, 50, or 100 mol% Ln^{3+} (Ln^{3+} = Dy^{3+}, Er^{3+}, or Yb^{3+}) were prepared via a hydrothermal method using oleic acid as capping ligands. The crystal phases of $BaGdF_5$: 50%Ln^{3+} (Ln^{3+} = Dy^{3+}, Er^{3+}, or Yb^{3+}) NPs were revealed by XRD patterns. As depicted in Figure 1b, all positions and intensities of the diffraction peaks of $BaGdF_5$: 50%Ln^{3+} (Ln^{3+} = Dy^{3+}, Er^{3+}, or Yb^{3+}) NPs were indexed to the standard cubic phase of $BaGdF_5$ crystal (JCPDS No.: 24-0098). There were no other impure diffraction peaks. The XRD results indicated that the doping ions were well incorporated in the Gd^{3+}-based host lattice. In contrast to cubic phase of $BaGdF_5$, a little shift of diffraction peaks towards higher angle direction was observed, which was due to the fact that the relative small ions, such as Dy^{3+} (1.167 Å), Er^{3+} (1.144 Å), or Yb^{3+} (1.125 Å), doped into Gd^{3+}-based (1.193 Å) host lattice.[60] Typical TEM images (Figure 1c-e) showed the near-spherical morphology and monodispersity of these Dy^{3+}, Er^{3+}, or Yb^{3+} doped $BaGdF_5$ NPs. Average diameters based on TEM results were calculated to be about 11, 15, and 14 nm for these $BaGdF_5$: 50%Ln^{3+} (Ln^{3+} = Dy^{3+}, Er^{3+}, or Yb^{3+}) NPs, respectively. The corresponding HR-TEM images (Figure S1a-c) show the measured interplanar distance of 2.86, 2.92, and 2.89 Å respectively, corresponding to the (200) crystal plane of cubic phase of $BaGdF_5$. SAED patterns of these NPs (Figure S1d-f) present the diffraction fringes of cubic phase, further confirming the above results from XRD. In addition, as shown in Figure S2, these $BaGdF_5$ NPs doped with 0 or 100% Ln^{3+} (Ln^{3+} = Dy^{3+}, Er^{3+}, or Yb^{3+}) also present uniform nanoparticle shape, cubic phase,

and monodispersity.

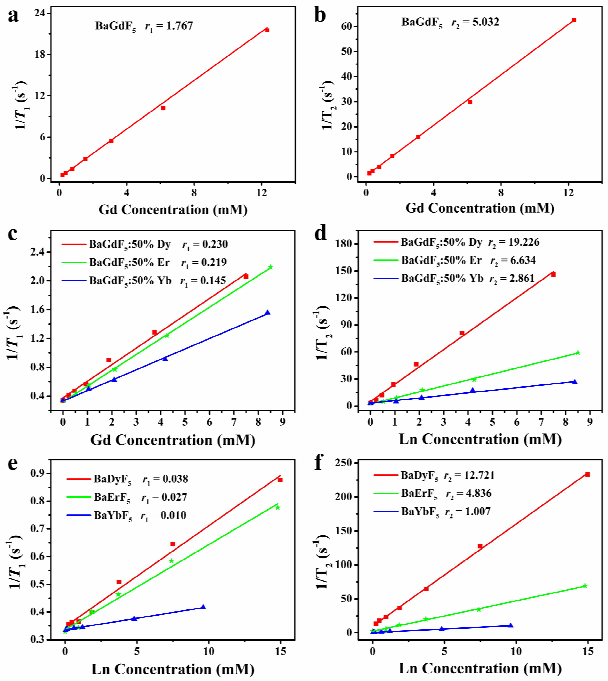

Figure 2. Longitude and transverse relaxivities studies of NPs. (a) r_1 and (b) r_2 values of pure $BaGdF_5$ NPs, (c) r_1 and (d) r_2 values of $BaGdF_5$:50 mol% Ln^{3+} (Ln^{3+} = Dy^{3+}, Er^{3+}, or Yb^{3+}) NPs, (e) r_1 and (f) r_2 values of $BaGdF_5$:100 mol% Ln^{3+} (Ln^{3+} = Dy^{3+}, Er^{3+}, or Yb^{3+}) NPs. The calculation is based on longitude and transverse relaxation rates versus Gd^{3+} or Ln^{3+} concentration. All measurements of T_1 and T_2 relaxation time are conducted by a 1.5 T MRI scanner.

3.2 Optimization of Longitude and Transverse Relaxivities

To investigate MRI performance of these single-phase $BaGdF_5$:x%Ln^{3+} (x= 0, 50, or 100; Ln^{3+} = Dy^{3+}, Er^{3+}, or Yb^{3+}) NPs, the hydrophobic NPs were converted to be hydrophilic ones using a diluted hydrochloric acid treatment.[57] After that, their T_1 and T_2 relaxivities measurements as well as the corresponding phantom studies were conducted using a 1.5 T MRI scanner. The as-prepared samples in aqueous solution with different Gd^{3+} or Ln^{3+} (Ln^{3+} = Dy^{3+}, Er^{3+}, or Yb^{3+}) concentrations were used for the measurement of r_1 and r_2 values based on the linear relationship of longitudinal and transverse relaxation rates versus concentrations of these magnetic mental ions. As shown in Figure 2a and b, r_1 and r_2 values of pure $BaGdF_5$ NPs were calculated to be 1.767 and 5.032 mM^{-1} s^{-1}, respectively, as well as the resulting r_2/r_1 value is 2.848. The high value of r_1 and reasonable value of r_2/r_1 make these pure $BaGdF_5$ NPs potentially positive contrast agents in T_1-weighted MRI. Plenty of Gd^{3+}-based NPs and compounds were developed for T_1-weighted MRI and even their clinical use.[2,56] However, these exploited agents, in general, only response to T_1-weighted imaging modality but not to T_2-weighted one. Therefore, we demostrated herein a general strategy for tuning the longitude and transverse relaxivities of Gd^{3+}-based NPs by using Ln^{3+}-doping method (Ln^{3+} = Dy^{3+}, Er^{3+}, or Yb^{3+}). This is due to the fact that Dy^{3+}, Er^{3+}, or Yb^{3+}-based NPs presented novel negative contrast effects in T_2-weighted MRI.[3,37-40] Besides, the magnetic moment of these ions (Dy^{3+}, μ_{eff} = 10.63 μ_B, high; Er^{3+}, μ_{eff} = 9.59 μ_B, mediate; Yb^{3+}, μ_{eff} = 4.53 μ_B, low)[55] changes in a large range, which contributes to realize tuning of relaxivities through doping them into Gd^{3+}-based NPs. As performed in Figure 2c, the r_1 values were 0.230, 0.219, and 0.145 mM^{-1} s^{-1} for 50% of Dy^{3+}, Er^{3+}, or Yb^{3+} doped $BaGdF_5$ NPs, respectively, which sharply reduced in contrast to that value of pure $BaGdF_5$ NPs. Besides, the tendency of the change among Ln^{3+}-doped NPs accords well with the magnetic moment of the dopants. Actually, superparamagnetic T_2 contrast resource can easily generate an induced magnetic field under an external magnetic field, and as a result affect the electronic spin of paramagnetic T_1 contrast resource.[21] The T_2 contrast resource increases the local magnetic field intensity of the T_1 contrast resource, and therefore makes an enhancement of T_1 relaxation rates. Under identical conditions for other parameters, doping Dy^{3+} with the highest magnetic moment has a greater impact on T_1 relaxation rates. While the positions of T_1 contrast resource (Gd^{3+}) was fully substituted by T_2 contrast resource (e.g., Dy^{3+}, Er^{3+}, or Yb^{3+}) in the host lattice, the r_1 values of these NPs absolutely decreased into a lower level (Figure 2e).

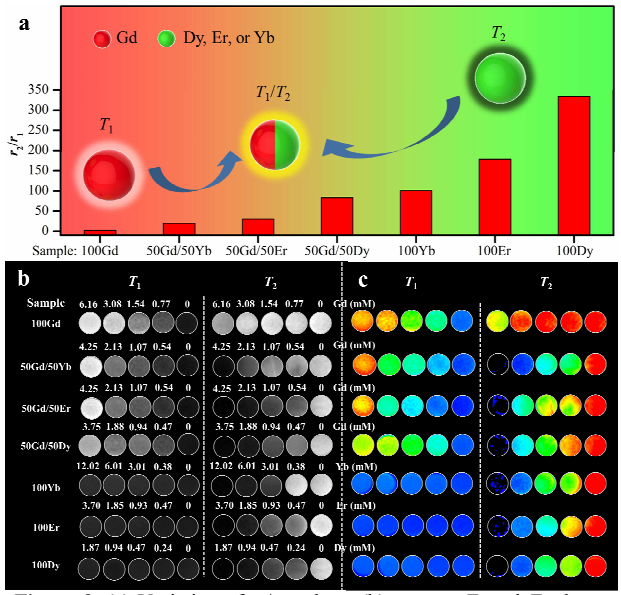

Figure 3. (a) Variation of r_2/r_1 values, (b) *in vitro* T_1 and T_2 phantom images of NPs and (c) their corresponding color images. The insets in a illustrate the formation of T_1/T_2 dual-weighted contrast agents via doping T_2 sources (Dy^{3+}, Er^{3+}, or Yb^{3+}) into T_1 one (Gd^{3+}). All these T_1 and T_2 phantom images are captured by a 1.5 T MRI scanner.

Apart from longitude relaxivity, doping large amounts (50 %) of Dy^{3+}, Er^{3+}, or Yb^{3+} can more efficiently affect transverse relaxation rates of these Gd^{3+}-based NPs. As shown in Figure 2d, the r_2 values of $BaGdF_5$:50%Ln^{3+} (Ln^{3+} = Dy^{3+}, Er^{3+}, or Yb^{3+}) NPs are 19.226, 6.634, and 2.861 mM^{-1} s^{-1}, respectively. The results reveal that the r_2 value of $BaGdF_5$ NPs can be largely tuned by doping these Ln^{3+} ions with different magnetic moments. Similarly, the r_2 values can also be finely-tuned when the Gd^{3+}-based host is absolutely replaced by Ln^{3+} doping (Figure 2f). As such, the control of transverse relaxivity with a wide range in $BaGdF_5$ host can be realized through a simple Ln^{3+} doping method, which mainly affects the r_2/r_1 values of these NPs. Moreover, the r_2/r_1 values increase from 2.8 to 334.8 when selecting different dopants and increasing their doping concentrations (Figure 3a). The undoped $BaGdF_5$ NPs can act as promising T_1 contrast agents for their calculated r_2/r_1 value (2.84, Figure 3a). This is due to the fact that r_2/r_1 value, no exceeding 3,

is considered to be suitable for acquiring positive contrast effects in general. The further *in vitro* phantom images (Figure 3b,c) reveal that these undoped $BaGdF_5$ NPs exhibit concentration-dependent contrast effect in T_1-weighted MRI, other than in T_2-weighted one. However, the r_2/r_1 values of the pure $BaYbF_5$, $BaErF_5$, and $BaDyF_5$ NPs are 100.7, 179.1, and 334.8, respectively. The extremely high r_2/r_1 values of these NPs make them promising T_2 contrast agents. The phantom images (Figure 3b,c) were also conducted to validate the abilities of these Ln^{3+}-based (Ln^{3+} = Dy^{3+}, Er^{3+}, or Yb^{3+}) NPs in T_1 or T_2-weighted MRI. As demonstrated, these pure Ln^{3+}-based NPs (Ln^{3+} = Dy^{3+}, Er^{3+}, or Yb^{3+}) only present T_2 contrast behavior. These results reveal that $BaGdF_5$:x mol%Ln^{3+} (x = 0 or 100, Ln^{3+} = Dy^{3+}, Er^{3+}, or Yb^{3+}) NPs can only be used as single-weighted agents in MRI. The r_2/r_1 values of $BaGdF_5$:50%Er^{3+} and $BaGdF_5$:50%Yb^{3+} NPs are calculated to be 30.3 and 19.7, respectively. And, the *in vitro* T_1 or T_2 phantom images exhibit obviously positive or negative contrast enhancing effects which rely on the increase of Ln^{3+} concentration in solution. These findings reveal that $BaGdF_5$ NPs doped with 50% Er^{3+} or Yb^{3+} could respond to dual-weighted MRI and may be emerged as synergistic contrast agents in both T_1 and T_2 MRI modalities. In addition, the r_2/r_1 value of $BaGdF_5$:50%Dy^{3+} NPs is high up to 83.6, and hence the T_2 phantom images of which show the concentration-dependent negative contrast effects. As expected, there is no obvious contrast changes of $BaGdF_5$:50%Dy^{3+} NPs in T_1 phantom images, which is mainly ascribed to a highly doping (50 mol%) prefers to form T_2 contrast effect owing to the large magnetic moment of Dy^{3+}. Therefore, we can easily realize the tuning of longitude and transverse relaxivities via doping Ln^{3+} (Ln^{3+} = Dy^{3+}, Er^{3+}, or Yb^{3+}) into $BaGdF_5$ NPs.

We selected $BaGdF_5$:50%Er^{3+} NPs as an example for further *in vivo* dual-weighted MRI investigations on the basis of their good performance in *in vitro* phantom images. Prior to applying these NPs to *in vivo* bioimaging, their cytotoxicity was tested. The *in vitro* cytotoxicity of $BaGdF_5$:50%Er^{3+} NPs in HeLa cells and HEK-293 cells was measured via 3-(4,5-dimethylthiazol-2-yl)-2,5 diphenyl-tetrazolium bromide (MTT) assays (Figure 4). The viability of Hela cells is above 79.5% when the concentration of these NPs is 500 μg/mL. Besides, the viability of HEK-293 cells is also not significantly affected by these NPs even as well at a relatively high dose at 500 μg/mL. The *in vitro* cell viability studies reveal the low cytotoxicity of these $BaGdF_5$:50%Er^{3+} NPs. In addition, *in vitro* hemolytic assay was also conducted to evaluate the interaction between NPs and blood components.[58,59] As illustrated in Figure 4c, almost no hemolysis of RBCs could be detected at the maximal experimental concentration (200 μg/mL), indicating the excellent blood compatibility of $BaGdF_5$:50%Er^{3+} NPs. Both MTT and *in vitro* hemolytic assays demonstrate that these NPs can be used as safe contrast agents for further *in vivo* MRI.

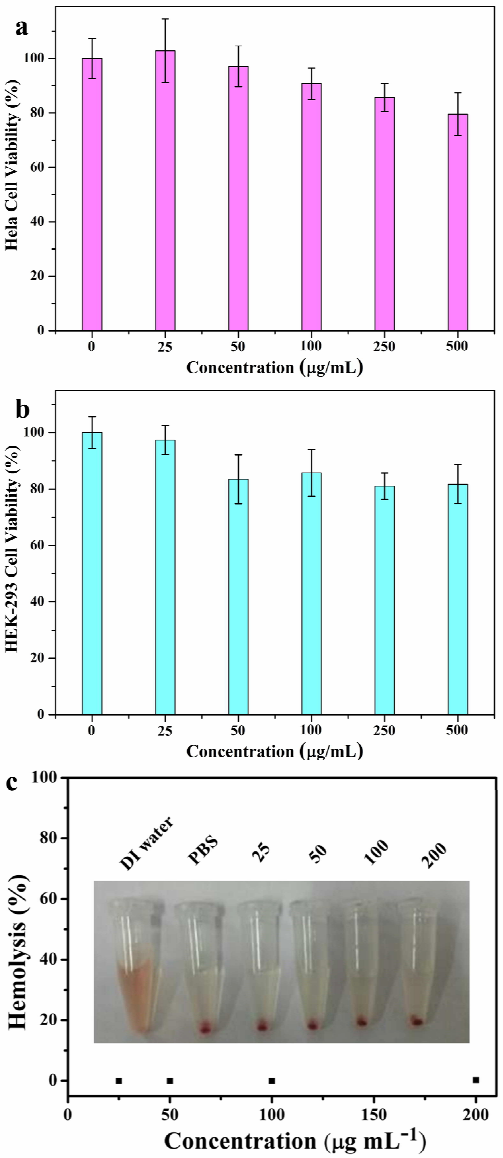

Figure 4. Cellular toxicity and in vitro hemolysis arrays of $BaGdF_5$: 50mol%Er^{3+} NPs. The viability of (a) Hela cells and (b) HEK-293 cells after treatment of various concentrations of NPs, (c) concentration dependent hemolysis. The insets in c are photographic images for direct observation of hemolysis.

3.3 Synergistic T_1/T_2 Dual-Weighted MRI and Their Tumor Detection

T_1/T_2 dual-weighted MRI has its great merits on improving diagnostic accuracy of disease through providing the comprehensive details of two modalities of images. After intravenous injection of $BaGdF_5$:50%Er^{3+} NPs, T_1 and T_2 dual modality whole-body images of mice are captured using corresponding imaging sequences in a MRI system. As illustrated in Figure 5a, the liver region (denoted by arrows) in the T_1 image shows slight contrast enhancement at 1 h after injection when compared with the signal before administration. Besides, the positive contrast effects in the liver location are enhanced after 3 h injection of NPs. In addition, weak signal enhancement also occurs in the intestines and stomach regions after 1 and 3 h injection of NPs. During the T_1 MRI detection, T_2 images of the

same mouse are also conducted using the same device. By contrast to the control image, the mouse presents obviously darker contrast in the liver region after 1 and 3 h injection of NPs. These findings demonstrate that our designed hybrid lanthanide NPs can present ideal binary contrast agents for simultaneous T_1/T_2 MRI.

To further study the feasibility of synergistic detection of tumor based on $BaGdF_5$:50%Er^{3+} NPs, tumor (HeLa cells) bearing mice under intravenous injection of NPs from tail vein are used for dual-weighted *in vivo* MRI. In T_1-weighted MRI (Figure 6a), the tumor site presents dark contrast before administration of our designed NPs. And after 3 h injection of NPs, the enhanced bright contrast in the tumor site is obviously observed, indicating the successfully T_1-weighted MRI guided tumor detection. By contrast, the tumor site shows the bright image initially and then becomes dark after injection of NPs in T_2-weighted MRI (Figure 6b). The high-contrast enhancement of tumor in dual-weighted MRI indicates that the injected $BaGdF_5$:50%Er^{3+} NPs can effectively uptake in the tumor site under blood circulation, which is based on enhanced permeability and retention (EPR) effect of NPs. Tumor detection via $BaGdF_5$:50%Er^{3+} NPs in dual-weighted MRI is achieved for the first time. In addition, the liver region (denoted by arrows) also exhibits a huge positive or negative contrast effect in T_1- or T_2-weighted MRI. More clear visualization of high-contrast effects in the tumor site and liver location can be observed from the corresponding images labeled with colors (Figure 6c,d). Moreover, it is noted that the injection of these $BaGdF_5$:50%Er^{3+} NPs can greatly enhance the visualization of the hepatic portal vein under T_2 weighted *in vivo* MRI. This phenomenon is mainly ascribed to the high accumulation of NPs and the resulting dark contrast enhancement in the liver parenchyma, leading to the convenient visualization of the vessel. These synergetic imaging results are matched well with the former analysis in the normal mice. Therefore, the obtained $BaGdF_5$:50%Er^{3+} NPs can be used as high-contrast and dual-modal agents in both T_1- and T_2-weighted MRI. And the synergistic imaging effects can provide more information details of the lesion, and as a result, improve the diagnostic accuracy of cancer.

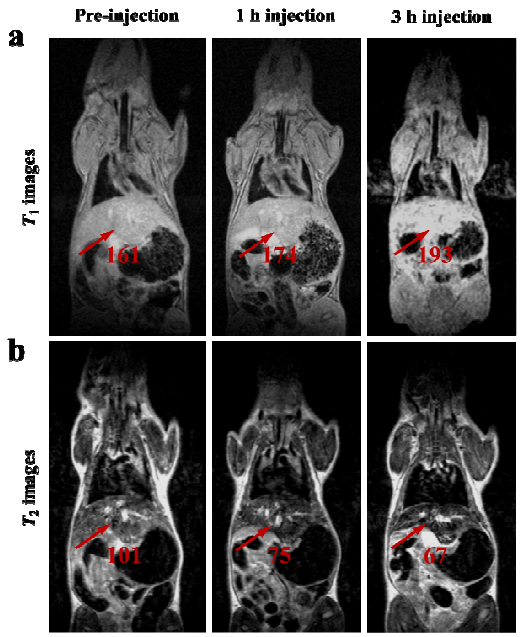

Figure 5. (a) T_1 and (b) T_2 weighted *in vivo* MRI coronal images of a healthy mouse before injection as well as 1 and 3 hours after intravenous injection of $BaGdF_5$:50 mol%Er NPs from tail vein. The arrows refer to the liver location with contrast enhancing effects and the numbers below are the corresponding average signal intensities. These *in vivo* MRI images are conducted by a 1.0 T MRI system.

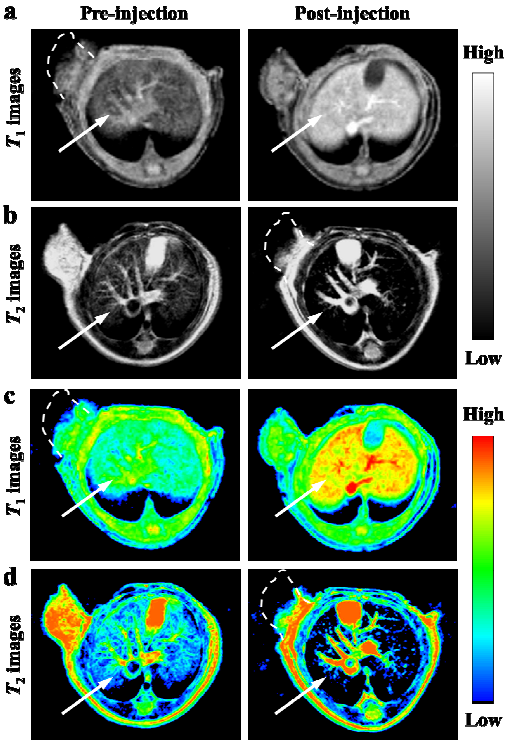

Figure 6. (a) T_1- and (b) T_2-weighted *in vivo* MRI transverse images of a tumor-bearing mouse before and 3 hours after intravenous injection of $BaGdF_5$:50 mol%Er NPs from tail vein. The arrows direct to the liver location and the dotted lines circle the tumor site, both regions of which present high-contrast effects in dual-weighted MRI. These *in vivo* MRI images are conducted by a 1.0 T MRI system.

4. Conclusion

In summary, we have demonstrated that longitudinal and transverse relaxivities of NPs can be tuned via a simple and efficient strategy by doping Ln^{3+} (Ln^{3+} = Dy^{3+}, Er^{3+}, or Yb^{3+} here) into $BaGdF_5$ host. These dopants with different magnetic moments majorly change T_2 relaxivities of NPs to achieve the control of r_2/r_1 values and contrast effects in dual-weighted MRI. The r_2/r_1 value of pure $BaGdF_5$ NPs can be readily adjusted from 2.8 to 19.7, 30.3 and 83.6 by doping 50 % of Ln^{3+} (Ln^{3+} = Yb^{3+}, Er^{3+}, or Dy^{3+}), respectively. When doping 100% Ln^{3+}, r_2/r_1 values are significantly enhanced to 334.8, indicating pure $BaLnF_5$ (Ln^{3+} = Yb^{3+}, Er^{3+}, or Dy^{3+}) NPs are ideal single T_2-weighted agents. Moreover, $BaGdF_5$ doped with 50 % Er^{3+} or Yb^{3+} NPs present dual-modal MRI behaviors in *in vitro* phantom experiments. The synergistic contrast enhancement of the liver region and tumor site in the live mice using $BaGdF_5$:50%Er^{3+} NPs can be realized by T_1/T_2 dual-weighted MRI *in vivo*. Therefore, $BaGdF_5$:50 %Er^{3+} NPs can be emerged as synergistic contrast enhancing agents for tumor detection in T_1/T_2 dual-weighted MRI. These findings provide a platform for designing synergistic T_1/T_2 dual-modal MRI agents to improve diagnostic accuracy by a general Ln^{3+}-doping method.

Acknowledgments

This work was supported by the National Natural Science Foundation of China (Nos. 51102202), specialized research Fund for the Doctoral Program of Higher Education of China (No. 20114301120006) and Hunan Provincial Natural Science Foundation of China (Nos. 12JJ4056 and 13JJ1017), Scientific Research Fund of Hunan Provincial Education Department (13B062) and CAS/SAFEA International Partnership Program for Creative Research Teams. We thank Dr. Hui Hui and Mr Xiao Liang in Key Laboratory of molecular Imaging, Chinese Academy of Sciences for *in vivo* MRI and helpful discussions.

Notes and references

[a] *College of Physics and Information Science and Key Laboratory of Low-dimensional Quantum Structures and Quantum Control of the Ministry of Education, Hunan Normal University, Changsha 410081, Hunan, China. Email: songjunz@hunnu.edu.cn*

[b] *School of Materials Science and Engineering, Key Laboratory of Low-dimensional Materials and Application Technology (Ministry of Education), Xiangtan University, Xiangtan 411105, China.*

[c] *Materials Research Center and Department of Applied Physics, The Hong Kong Polytechnic University, Hong Kong.* *Email: jh.hao@polyu.edu.hk

[d] *These authors contributed equally to this paper.*

1. R. Weissleder and M. J. Pittet, *Nature*, 2008, **452**, 580.
2. J. S. Ananta1, B. Godin, R. Sethi, L. Moriggi, X. W. Liu, R. E. Serda, R. Krishnamurthy, R. Muthupillai, R. D. Bolskar, L. Helm, M. Ferrari, L. J. Wilson and P. Decuzzi, *Nat. Nanotech.*, 2010, **5**, 815.
3. G. K. Das, N. J. J. Johnson, J. Cramen, B. Blasiak, P. Latta, B. Tomanek and F. C. J. M. van Veggel, *J. Phys. Chem. Lett.*, 2012, **3**, 524.
4. R. Kumar, M. Nyk, T. Y. Ohulchanskyy, C. A. Flask and P. N. Prasad, *Adv. Funct. Mater.*, 2009, **19**, 853.
5. Z. H. Zhao, X. M. Wang, Z. J. Zhang, H. Zhang, H. Y. Liu, X. L. Zhu, H. Li, X. Q. Chi, Z. Y. Yin and J. H. Gao, *ACS Nano*, 2015, **9**, 2749.
6. Y. J. Chen, H. C. Gu, D. S. Zhang, F. Li, T. Y. Liu and W. L. Xia, *Biomaterials*, 2014, **35**, 10058.
7. R. P. Mason, D. Zhao, J. Pacheco-Torres, W. Cui, V. D. Kodibagkar, P. K. Gulaka, G. Hao, P. Thorpe, E. W. Hahn and P. Peschke, *Q. J. Nucl. Med. Mol. Imaging*, 2010, **54**, 259.
8. M. Bottrill, L. Kwok and N. J. Long, Chem. Soc. Rev., 2006, 35, 557.
9. K. N. Raymond and V. C. Pierre, *Bioconjug Chem.*, 2004, **16**, 3.
10. J. S. Kim, W. J. Rieter, K. M. L. Taylor, H. Y. An, W. L. Lin and W. B. Lin, *J. Am. Chem. Soc.*, 2007, **129**, 8962.
11. B. H. Kim, N. Lee, H. Kim, K. An, Y. I. Park, Y. Choi, K. Shin, Y. Lee, S. G. Kwon, H. B. Na, J. G. Park, T. Y. Ahn, Y. W. Kim, W. K. Moon, S. H. Choi and T. Hyeon, *J. Am. Chem. Soc.*, 2011, **133**, 12624.
12. U. I. Tromsdorf, O. T. Bruns, S. C. Salmen, U. Beisiegel and H. Weller, *Nano Lett.*, 2009, **9**, 4434.
13. K. Dong, Z. Liu, J. H. Liu, S. Shuang, Z. H. Li, Q. H. Yuan, J. S. Ren and X. G. Qu, *Nanoscale*, 2014, **6**, 2211.
14. H. B. Na, J. H. Lee, K. An, Y. I. Park, M. Park, I. S. Lee, D. H. Nam, S. T. Kim, S. H. Kim, S. W. Kim, K. H. Lim, K. S. Kim, S. O. Kim and T. Hyeon, *Angew. Chem. Int. Ed.*, 2007, **46**, 5397.
15. H. Yang, Y. M. Zhuang, H. Hu, X. X. Du, C. X. Zhang, X. Y. Shi, H. X. Wu and S. P. Yang, *Adv. Funct. Mater.*, 2010, **20**, 1733.
16. T. Kim, E. Momin, J. Choi, K. Yuan, H. Zaidi, J. Kim, M. Park, N. Lee, M. T. McMahon, A. Quinones-Hinojosa, J. W. M. Bulte, T. Hyeon and A. A. Gilad, *J. Am. Chem. Soc.*, 2011, **133**, 2955.
17. Y. W. Jun, J. H. Lee and J. Cheon, *Angew. Chem. Int. Ed.*, 2008, **47**, 5122.
18. J. Park, K. An, Y. Hwang, J. G. Park, H. J. Noh, J. Y. Kim, J. H. Park, N. M. Hwang and T. Hyeon, *Nat. Mater.*, 2004, **3**, 891.
19. J. H. Lee, Y. M. Huh, Y. W. Jun, J. W. Seo, J. T. Jang, H. T. Song, S. Kim, E. J. Cho, H. G. Yoon, J. S. Suh and J. Cheon, *Nat. Med.*, 2007, **13**, 95.
20. W. S. Seo, J. H. Lee, X. Sun, Y. Suzuki, D. Mann, Z. Liu, M. Terashima, P. C. Yang, M. V. McConnell, D. G. Nishimura and H. Dai, *Nat. Mater.*, 2006, **5**, 971.
21. Z. J. Zhou, D. T. Huang, J. F. Bao, Q. L. Chen, G. Liu, Z. Chen, X. Y. Chen and J. H. Gao, *Adv. Mater.*, 2012, **24**, 6223.
22. W. C. Xiao, J. Lin, M. L. Li, Y. J. Ma, Y. X. Chen, C. F. Zhang, D. Li and H. C. Gu, *Contrast Media. Mol. I.*, 2012, **7**, 320.
23. M. Valko, H. Morris and M. T. D. Cronin, *Curr. Med. Chem.*, 2005, **12**, 1161.
24. K. Jellinger, W. Paulus, I. Grundke-Iqbal, P. Riederer and M. B. H. Youdim, *J. Neural Transm.*, 1990, **2**, 327.
25. H. B. Na, I. C. Song and T. Hyeon, *Adv. Mater.*, 2009, **21**, 2133.
26. J. W. M. Bulte and D. L. Kraitchman, *NMR Biomed.*, 2004, **17**, 484.
27. J. S. Choi, J. H. Lee, T. H. Shin, H. K. Song, E. Y. Kim and J. Cheon, *J. Am. Chem. Soc.*, 2010, **132**, 11015.
28. G. H. Im, S. M. Kim, D. G. Lee, W. J. Lee, J. H. Lee and I. S. Lee, *Biomaterials*, 2013, **34**, 2069.
29. H. Y. Chen, B. Qi, T. Moore, D. C. Colvin, T. Crawford, J. C. Gore, F. Alexis, O. T. Mefford and J. N. Anker, *Small*, 2014, **10**, 160.
30. J. Chen, W. J. Zhang, Z. Guo, H. B. Wang, D. D. Wang, J. J. Zhou and Q. W. Chen, *ACS Appl. Mater. Interfaces*, 2015, **7**, 5373.
31. L. J. Yang, Z. J. Zhou, H. Y. Liu, C. Q. Wu, H. Zhang, G. M. Huang, H. Ai and J. H. Gao, *Nanoscale*, 2015, **7**, 6843.
32. Z. J. Zhou, C. Q. Wu, H. Y. Liu, X. L. Zhu, Z. H. Zhao, L. R. Wang, Y. Xu, H. Ai and J. H. Gao, *ACS Nano*, 2015, **9**, 3012.
33. H. Yang, Y. M. Zhuang, Y. Sun, A. T. Dai, X. Y. Shi, D. M. Wu, F. Y. Li, H. Hu and S. P. Yang, *Biomaterials*, 2011, **32**, 4584.
34. K. Cheng, M. Yang, R. P. Zhang, C. X. Qin, X. H. Su and Z. Cheng, *ACS Nano*, 2014, **8**, 9884.
35. K. H. Bae, Y. B. Kim, Y. Lee, J. Hwang, H. Park and T. G. Park, *Bioconjug Chem.*, 2010, **21**, 505.
36. X. Y. Wang, Z. J. Zhou, Z. Y. Wang, Y. X. Xue, Y. Zeng, J. H. Gao, L. Zhu, X. Z. Zhang, G. Liu and X. Y. Chen, *Nanoscale*, 2013, **5**, 8098.
37. D. L. Ni, W. B. Bu, S. J. Zhang, X. P. Zheng, M. Li, H. Y. Xing, Q. F. Xiao, Y. Y. Liu, Y. Q. Hua, L. P. Zhou, W. J. Peng, K. L. Zhao and J. L. Shi, *Adv. Funct. Mater.*, 2014, **24**, 6613.
38. I. Bertini, F. Capozzi, C. Luchinat, G. Nicastro and Z. C. Xia, *J. Phys. Chem.*, 1993, **97**, 6351.

39. K. Kattel, J. Y. Park, W. Xu, H. G. Kim, E. J. Lee, B. A. Bony, W. C. Heo, J. J. Lee, S. Jin, J. S. Baeck, Y. Chang, T. J. Kim, J. E. Bae, K. S. Chae and G. H. Lee, *ACS Appl. Mater. Interfaces*, 2011, **3**, 3325.
40. H. B. Wang, W. Lu, T. M. Zeng, Z. G. Yi, L. Rao, H. R. Liu and S. J. Zeng, *Nanoscale*, 2014, **6**, 2855.
41. F. Wang and X. G. Liu, *Chem. Soc. Rev.*, 2009, **38**, 976.
42. J. Zhou, Z. Liu and F. Y. Li, *Chem. Soc. Rev.*, 2012, **41**, 1323.
43. Z. G. Yi, W. Lu, Y. R. Xu, J. Yang, L. Deng, C. Qian, T. M. Zeng, H. B. Wang, L. Rao, H. R. Liu and S. J. Zeng, *Biomaterials*, 2014, **35**, 9689.
44. K. Z. Zheng, G. H. He, W. Y. Song, X. Q. Bi and W. P. Qin, *J. Mater. Chem. C*, 2015, **3**, 11589.
45. Z. Liu, Z. H. Li, J. H. Liu, S. Gu, Q. H. Yuan, J. S. Ren and X. G. Qu, *Biomaterials*, 2012, **33**, 6748.
46. Z. G. Yi, X. L. Li, Z. L. Xue, X. Liang, W. Lu, H. Peng, H. R. Liu, S. J. Zeng and J. H. Hao, *Adv. Funct. Mater.*, 2015, **25**, 7119.
47. S. J. Zeng, M. K. Tsang, C. F. Chan, K. L. Wong and J. H. Hao, *Biomaterials*, 2012, **33**, 9232.
48. L. Zhou, R. Wang, C. Yao, X. M. Li, C. L. Wang, X. Y. Zhang, C. J. Xu, A. J. Zeng, D. Y. Zhao and F. Zhang, *Nat. Commun.*, 2015, **6**, 6938.
49. (a) F. Chen, W. B. Bu, S. J. Zhang, J. N. Liu, W. P. Fan, L. P. Zhou, W. J. Peng and J. L. Shi, *Adv. Funct. Mater.*, 2013, **23**, 298; (b) G. V. Martinez, X. M. Zhang, M. L. Garcia-Martin, D. L. Morse, M. Woods, A. D. Sherry and R. J. Gillies, *NMR In Biomedicine*, 2011, **24**, 1380.
50. F. Wang, Y. Han, C. S. Lim, Y. H. Lu, J. Wang, J. Xu, H. Y. Chen, C. Zhang, M. H. Hong and X. G. Liu, *Nature*, 2010, **463**, 1061.
51. Z. G. Yi, W. Lu, H. R. Liu and S. J. Zeng, *Nanoscale*, 2015, **7**, 542.
52. S. J. Zeng, Z. G. Yi, W. Lu, C. Qian, H. B. Wang, L. Rao, T. M. Zeng, H. R. Liu, H. J. Liu, B. Fei and J. H. Hao, *Adv. Func. Mater.*, 2014, **24**, 4196.
53. L. Vander Elst, A. Roch, P. Gillis, S. Laurent, F. Botteman, J. W. Bulte and R. N. Muller, *Magn. Reson. Med.*, 2002, **47**, 1121.
54. Z. Kovacs, K. N. Green, S. J. Ratnakar and A. D. Sherry, *Chem. Rev.*, 2010, **110**, 2960.
55. M. Norek and J. A. Peters, *Prog. Nucl. Magn. Reson. Spectrosc.*, 2011, **59**, 64.
56. P. Caravan, J. J. Ellison, T. J. McMurry and R. B. Lauffer, *Chem. Rev.*, 1999, **99**, 2293.
57. N. Bogdan, Vetrone, G. A. Ozin and J. A. Capobianco, *Nano Lett.*, 2011, **11**, 835.
58. Z. Liu, F. Pu, S. Shuang, Q. H. Yuan, J. S. Ren and X. G. Qu, *Biomaterials*, 2013, **34**, 1712.
59. K. Dong, E. G. Ju, J. H. Liu, X. L. Han, J. S. Ren and X. G. Qu, *Nanoscale*, 2014, **6**, 12042.
60. R. D. Shannon, *Acta Cryst.*, 1976, **A32**, 751.

Hybrid lanthanide nanoparticles as a new class of binary contrast agents for *in vivo* T_1/T_2 dual-weighted MRI and synergistic tumor diagnosis

Zhigao Yi, Xiaolong Li, Wei Lu, Hongrong Liu, Songjun Zeng, and Jianhua Hao**

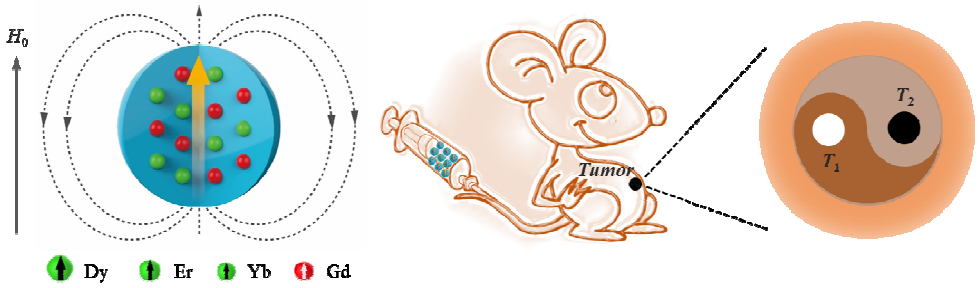

A new type of hybrid lanthanide nanoparticles have been demonstrated as synergistic contrast agents in T_1/T_2 dual-weighted MRI and the imaging directed tumor diagnosis.